

Coexistence of Tri-Hexagonal and Star-of-David Pattern in the Charge Density Wave of the Kagome Superconductor AV_3Sb_5

Yong Hu^{1,*}, Xianxin Wu^{2,3,*}, Brenden R. Ortiz⁴, Xinloong Han⁵, Nicholas C. Plumb¹, Stephen D. Wilson⁴, Andreas P. Schnyder², and Ming Shi^{1,*}

¹Swiss Light Source, Paul Scherrer Institute, CH-5232 Villigen PSI, Switzerland

²Max-Planck-Institut für Festkörperforschung, Heisenbergstrasse 1, D-70569 Stuttgart, Germany

³CAS Key Laboratory of Theoretical Physics, Institute of Theoretical Physics, Chinese Academy of Sciences, Beijing 100190, China

⁴Materials Department, University of California Santa Barbara, Santa Barbara, California 93106, USA

⁵Kavli Institute of Theoretical Sciences, University of Chinese Academy of Sciences, Beijing, 100049, China

*To whom correspondence should be addressed:

Y.H. (yonghphysics@gmail.com); X.W. (xianxin.wu@fkf.mpg.de); M.S. (ming.shi@psi.ch).

The recently discovered layered kagome metals AV_3Sb_5 ($A=K, Rb, Cs$) have attracted much attention because of their unique combination of superconductivity, charge density wave (CDW) order, and nontrivial band topology. The CDW order with an in-plane 2×2 reconstruction is found to exhibit exotic properties, such as time-reversal symmetry breaking and rotational symmetry breaking. However, the nature of the CDW, including its dimensionality, structural pattern, and effect on electronic structure, remains elusive despite intense research efforts. Here, using angle-resolved photoemission spectroscopy, we unveil for the first time characteristic double-band splittings and band reconstructions, as well as the band gap resulting from band folding, in the CDW phase. Supported by density functional theory calculations, we unambiguously show that the CDW in AV_3Sb_5 originates from the intrinsic coexistence of Star-of-David and Tri-Hexagonal distortions. The alternating stacking of these two distortions naturally leads to three-dimensional $2\times 2\times 2$ or $2\times 2\times 4$ CDW order. Our results provide crucial insights into the nature and distortion pattern of the CDW order, thereby laying down the basis for a substantiated understanding of the exotic properties in the family of AV_3Sb_5 kagome metals.

Transition-metal-based kagome materials, owing to the unique lattice geometry, provide a fascinating platform to study spin liquid states [1-6], flat bands [7], superconductivity [8-11], charge density wave (CDW) order [9-13] and topological physics [14-17]. Recently, the discovery of a new class of kagome metals AV_3Sb_5 ($A=K, Rb, Cs$), exhibiting topologically non-trivial electronic structure, unconventional superconductivity and CDW order, have been attracting tremendous attention [18-52]. Superconductivity emerges with a critical temperature $T_C \sim 0.9-2.5$ K at ambient pressure [19-21]. Subsequent investigations reveal a significant residual thermal conductivity [27], double superconducting domes under pressure [28-30], and an edge supercurrent in $Nb/K_{1-x}V_3Sb_5$ [31], indicating possible unconventional superconductivity. A CDW phase transition occurs at $T_{CDW} \sim 78-103$ K [19,21,32], for which scanning tunneling microscopy (STM) suggested a broken translation symmetry with a 2×2 in-plane reconstructions [32-34] and broken time-reversal symmetry [32,35]. In addition, an enhanced relaxation rate in the CDW phase from recent zero-field μ SR experiments is in line with a broken time-reversal symmetry [35], which could be intimately related to the observed giant anomalous Hall effect [36,37]. Furthermore, CDW order possessing lattice rotational symmetry breaking [38] can be inferred owing to the two-fold symmetrical c -axis resistivity from magneto-resistance measurements [39]. Theoretical studies provide two scenarios about the in-plane CDW order: phonon softening [40,41] and interaction-driven Fermi surface instability [42-44].

In addition to the in-plane reconstruction, X-ray diffraction (XRD) and STM experiments further reveal modulation along the c -direction [32,45], implying a three-dimensional (3D) CDW order. The charge modulation shows a π -phase shift across the single-unit-cell step edge in STM measurements, suggesting a $2 \times 2 \times 2$ CDW order [46]. However, recent XRD measurements suggest a $2 \times 2 \times 4$ reconstruction [47] and even a transition between these two by varying temperature [48]. Moreover, the CDW structural pattern is still unclear: NMR measurements tend to suggest a Star of David (SoD) distortion, [49] although the Tri-Hexagonal (TrH) distortion is theoretically more stable [40,41]. Despite the experimental evidence for a 3D CDW order, direct spectroscopic evidence about the reconstruction of the vanadium d -orbitals associated with the kagome lattice in AV_3Sb_5 is still lacking, which is crucial for revealing the CDW pattern in the system. A detailed understanding of the 3D CDW structural pattern, and in particular the ensuing electronic structure reconstruction, are of crucial importance for understanding the nature and origin of the CDW order and its interplay with superconductivity.

In this work, we used polarization- and temperature-dependent angle-resolved photoemission spectroscopy (ARPES) to reveal the nature of the CDW in the kagome superconductors AV_3Sb_5 from an electronic perspective. Upon cooling, the energy location of the two near- E_F VHSs is found to suddenly drop by about 90 meV, once the temperature falls below T_{CDW} . Moreover, universal band-splitting-like features on the kagome bands are revealed, exhibiting prominent band-folding effects in the kagome lattice, which can be well captured by the DFT calculations including superimposed Tri-Hexagonal and Star-of-David CDW patterns. The characteristic splittings from the two patterns can be experimentally extracted, and they are almost quantitatively consistent with calculations, clearly demonstrating intrinsic coexistence of two patterns in the CDW order. These findings not only provide essential insights into the band reconstructions of the CDW order but also unambiguously identify the 3D nature and CDW distortion pattern, which will be crucial in illuminating its mechanism.

The pristine phase of CsV_3Sb_5 crystallizes in a layered crystal structure with the space group $P6/mmm$ (No. 191) (Fig. 1a). It consists of V_3Sb kagome layers bounded above and below by Sb honeycomb layers and Cs hexagonal networks [Fig. 1a(i)]. Below the CDW transition temperature ($T_{CDW} = 94$ K), the kagome layer can exhibit two types of distortions derived from breathing phonon modes [39]: a Star of David [Fig. 1b(i)] and its inverse structure (Tri-Hexagonal) [Fig. 1b(ii)]. The orbital-resolved band structure of pristine CsV_3Sb_5 from DFT calculations is shown in Fig. 1c, where Sb p_z orbital contributes an electron band around the Brillouin zone (BZ) center and vanadium d orbitals dominate the Dirac cone (DC) bands around the K point and fourfold van Hove singularity (VHS) bands around the M point with diverse sublattice features. To demonstrate the effect of CDW order on the electronic structure, we first compare the ARPES spectra of CsV_3Sb_5 in the normal state ($T \gg T_{CDW}$) and CDW phase ($T \ll T_{CDW}$). Figure 1d plots the constant energy contours (CECs) and their evolution with binding energy (E_B). With increasing E_B , the Sb contributed circular-shaped pocket near the zone center (Γ) and triangle-shaped Fermi surface (FS) derived from the vanadium kagome lattice around the \bar{K} points shrink [(Fig. 1d(i-iii))], reflecting their electron-like nature. In the CDW states ($T \ll T_{CDW}$), one prominent change is that the electron pocket around $\bar{\Gamma}$ is doubled [Figs. 1b(i-iii)], which has been suggested to originate from the k_z broadening of the Sb p_z orbital [50], quantum well states on the surface [51], or the out-of-plane band folding [52]. Moreover, the triangle-shaped CECs associated with the vanadium d orbital around \bar{K} enlarge slightly in the CDW phase [Figs. 1e(i-iii)], compared with the corresponding CECs at the same E_B in the normal state [Fig. 1d(i-iii)]. To further identify the

effect of CDW order, we compare the band dispersions along the $\bar{\Gamma}$ - \bar{K} - \bar{M} - $\bar{\Gamma}$ direction above and below the T_{CDW} . ARPES spectra reveal a downward shift of the bands around \bar{M} point in the CDW phase [Figs. 1f(i) and 1g(i)], which is more evident with linear vertically (LV) polarized light [see the arrows in Figs. 1f(ii) and 1g(ii)]. The Dirac-like crossing point between $\bar{\Gamma}$ and \bar{K} point also shifts down significantly in energy in the CDW state, as indicated by the arrows in Figs. 1f(iii) and 1g(iii) (for details, see Supplementary Fig. S1). Since there are multiple VHSs located around the \bar{M} point (Fig. 1c) [24], carrying large density of states, the CDW-induced band reconstruction on them could be prominent.

To further demonstrate the salient features of the band reconstruction at the VHSs in the CDW phase, we performed systematic temperature- and polarization-dependent measurements on CsV_3Sb_5 along the $\bar{\Gamma}$ - \bar{K} - \bar{M} - \bar{K} and $\bar{\Gamma}$ - \bar{M} - $\bar{\Gamma}$ directions (Fig. 2). Upon cooling, the overall evolution of the band structures can be divided into two distinct regions: above and below the T_{CDW} . As show in Fig. 2a, above T_{CDW} ($T = 200$ K, 110 K), the band dispersion remains almost unchanged (Figs. 2a and 2b), while once below T_{CDW} ($T = 87$ K, 20 K), the pronounced band reconstruction around \bar{M} can be observed [Figs. 2c and 2d, as highlighted by the pink box in Fig. 2d(i)]. To clearly disentangle the bands and keep track of the energy location of the VHSs, we show the polarization dependence of the spectra in Figs. 2e-2l. Cooling from the normal state ($T \gg T_{CDW}$) to the CDW phase ($T \ll T_{CDW}$), VHS1 band exhibits unusual spectral broadening and energy shift along the \bar{K} - \bar{M} direction in the CDW phase [Figs. 2e-2f(i)], which is further accentuated by the temperature-dependent energy distribution curves (EDCs) taken near the flat feature of VHS1 (Fig. 2m). Under our ARPES geometry, VHS2 bands (d_{yz} orbital) along the $\bar{\Gamma}$ - \bar{K} [Figs. 2e-2h(i)] and $\bar{\Gamma}$ - \bar{M} [Figs. 2e-2h(ii)] directions are detected by linear horizontal (LH) and LV polarized light, respectively [24], while the VHS4 bands with d_{xz} character along the $\bar{\Gamma}$ - \bar{K} [Figs. 2i-2l(i)] and $\bar{\Gamma}$ - \bar{M} [Figs. 2i-2l(ii)] paths are favored under the LH and LV polarizations, respectively (for details, see Supplementary Fig. S2). The energy location of VHS2 (resp. VHS4) is determined by the d_{xz} band top (resp. d_{yz} -band bottom) along $\bar{\Gamma}$ - \bar{K} and its band bottom (resp. band top) along $\bar{\Gamma}$ - \bar{M} direction. Figure 2n shows the temperature dependence of the energy locations of VHS2 and VHS4, which suddenly drop in energy across the CDW transition by about 90 meV. Notably, the dichotomy between VHSs bands with different V d -orbital characters (Figs. 2m and 2n) indicates that the band reconstruction in the CDW phase is orbitally-selective (also see Supplementary Fig. S3). The band shifts take place suddenly when the system enters the CDW

phase (Fig. 2), suggesting that they are intimately related to the CDW order and the CDW transition is first order.

Besides the energy shift of the VHSs, we further display the characteristic double-band splitting features on the vanadium d -orbitals of the CDW phase in detail along high-symmetry paths (Figs. 3a-3f). In Figs. 3a and 3b, we show the temperature dependence of the ARPES spectra collected under circular (C) polarization along the $\bar{\Gamma} - \bar{K} - \bar{M}$ direction. Remarkably, compared to the bands measured above T_{CDW} ($T = 110\text{ K}, 200\text{ K}$), the spectra taken below T_{CDW} ($T = 20\text{ K}, 87\text{ K}$) exhibit diverse band-splitting-like features on the d -orbital bands in almost the entire energy-momentum space [indicated by the red dashed line and arrow in Fig. 3b(i)]. Specifically, splittings occur near the Fermi level (BS1), on the lower branch of the Dirac cone band along the $\bar{\Gamma} - \bar{M}$ direction (marked as BS2, B3), around the VHS3 bands (BS4), and even on the bands with an E_B lower than 1.0 eV (BS5, BS6). Consistently, the double-band splittings can also be clearly seen in the bands measured at low temperature (Figs. 3d and 3e), along the $\bar{\Gamma} - \bar{M}$ direction [marked as BS7-BS9 in Fig. 3e(i), for details, see Fig. S3]. By showing the ARPES spectra below and above T_{CDW} in the same plot, Figures 3c and 3f highlight the marked contrast between the bands in the normal state and CDW phase. Besides the double-band splitting features, below the T_{CDW} , CDW folding gaps of the d_{xy} band can be identified along the $\bar{\Gamma} - \bar{K}$ direction [indicated by the blue arrow in Fig. 3c(ii)], which is consistent with the observation in KV_3Sb_5 [25]. Moreover, we have checked the band structure of RbV_3Sb_5 in the CDW phase, and found a similar band reconstruction (i.e., the double-band splittings and folding gaps, see Supplementary Fig. S4 for details). Therefore, the temperature- and material-dependent ARPES spectra (Figs. 3a-3e and Fig. S4) strongly demonstrate that the observed double-band splitting features are directly derived from the CDW order. However, these features cannot be explained by an in-plane CDW order. As shown Fig. 3g, we show the unfolded band structure of CsV_3Sb_5 by considering the 2×2 TrH reconstruction [Fig. 1b(ii)]. While the two-dimensional (2D) lattice reconstruction can only qualitatively capture the folding gap along the $\bar{\Gamma} - \bar{K}$ direction [see the blue arrow in Figs. 3c(ii) and 3g], the new emergent bands observed in the CDW phase are completely missing.

Motivated by the suggested $2 \times 2 \times 2$ CDW order from recent XRD and STM measurements in AV_3Sb_5 kagome metals, we further explore the band reconstructions from a 3D CDW order. Actually, the

SoD- or TrH-like distortion in the vanadium kagome layers can induce an A_{1g} out-of-plane distortion of the Sb atoms, which naturally introduces interlayer coupling between kagome layers and generates a genuine 3D CDW distortion. For the $2 \times 2 \times 2$ CDW order, consisting of SoD- or TrH-like distortions, there are four possible configurations along the c axis: SoD- π , TrH- π , SoD-TrH- π and SoD-TrH, where π denotes an in-plane π -phase shift between adjacent kagome layers (see Fig. S5 for details). It is noted that the six-fold rotation symmetry is broken in the former three configurations and the point group is reduced to D_{2h} , while all symmetries of the original lattice are preserved in the last one. The unfolded band dispersions for the SoD- π and TrH- π configurations are displayed in Figs. 4a and 4b, respectively (dispersion along other paths can be found in Supplementary Fig. S6 and S7, and there is no qualitative difference). In the SoD- π configuration, the VHS1, VHS2 and VHS4 bands around \bar{M} point are gapped (indicated by the green arrow in Figs. 4a and 4b). In addition, two folding gaps for the d_{xy} band along the $\bar{\Gamma} - \bar{K}$ direction above and below the band crossing can be clearly identified (marked as the black arrow in Figs. 4a and 4b). The band reconstruction in the TrH- π configuration is similar but with much larger splitting and gap, especially for the VHS1 and VHS2 bands. However, these band reconstructions are similar to those from 2D SoD or TrH distortions except for some noticeable band folding around $\bar{\Gamma}$, and thus cannot explain the doubled-splitting features in experiments. We further display the unfolded band dispersion for the structures with alternating SoD- and TrH-like distortions in Figs. 4c (SoD-TrH- π) and 4d (SoD-TrH). The band dispersion in both cases is relatively similar and the band reconstruction consists of contributions from both SoD- and TrH-like distortions, generating double-splitting features. Interestingly, the splitting of the lower Dirac cone bands along the $\bar{K} - \bar{M}$ can be clearly identified (marked as BS2 in Figs. 4d and 4e). By comparing Fig. 4e and Figs. 4c,4d, we find that the observed band reconstructions (BS1, BS2, BS4, BS5, BS7-BS9) in our ARPES experiments can be well reproduced from these two distortions. As the SoD- and TrH-like distortions exhibit distinct splittings and folding gaps, we can further extract the energy scales of the splitting Δ_1 around \bar{M} point, the CDW folding gap Δ_2 along the $\bar{K} - \bar{M}$ direction, the flat $d_{xy}/d_{x^2-y^2}$ -band splitting Δ_3 , and the near- E_F -band splitting Δ_4 , for CsV_3Sb_5 in experiments. We summarize the experimental values in Table I, in comparison to theoretical values for four different configurations. It is striking that the experimental values are in very good agreement with the theoretical values of the SoD-TrH- π and SoD-TrH configurations. Intriguingly, the double-band splitting on the d_{xy} band along the $\bar{\Gamma} - \bar{K}$ direction (BS3 and BS6) can be better captured by the SoD-TrH configuration. However, this feature can be also reproduced along

other paths in the SoD-TrH- π configuration (for details, see Supplementary Fig. S7), where the six-fold rotational symmetry is broken. Therefore, from our ARPES measurement, both configurations are possible, which is further supported by their close energies in theoretical calculations (less than 1 meV/f.u.).

Table I: The experimentally determined energy scales of the double-band splittings, and their comparison with theoretical values.

	Exp.	SoD- π	TrH- π	SoD-TrH- π	SoD-TrH
Δ_1^{SoD}	70 meV	105 meV		130 meV	90 meV
Δ_1^{TrH}	200 meV		220 meV	230 meV	210 meV
Δ_2^{SoD}	120 meV	120 meV		210 meV	160 meV
Δ_2^{TrH}	170 meV		210 meV	210 meV	220 meV
Δ_3	110 meV	120 meV	270 meV	170 meV	130 meV
Δ_4	90 meV	60 meV	240 meV	100 meV	100 meV

Our ARPES measurements, combined with DFT calculations, for the first time, unambiguously reveal band reconstructions originating from both SoD- and TrH-like distortions. This demonstrates the coexistence of the two distortions in the CDW phase, although the SoD phase is theoretically believed to be metastable. These distortions lead to strong reconstructions of both the VHS bands and the vanadium d -orbital bands (especially for $d_{xy}/d_{x^2-y^2}$ bands). The stacking of the two distortions along the c axis can generate a 3D CDW order. Their alternating stacking yields a 2x2x2 CDW order. More complicated stacking, such as T $\bar{\text{S}}\bar{\text{T}}\bar{\text{S}}$ and TTST, where $\bar{\text{T}}$ or $\bar{\text{S}}$ denotes an in-plane π shift, can quadruple the unitcell along the c axis and lead to a 2x2x4 CDW order (see Supplementary Fig. S8 for the bands structure of T $\bar{\text{S}}\bar{\text{T}}\bar{\text{S}}$ stacking), which is suggested by recent XRD measurements [47,48]. In the CDW phase, the experimental transition between 2x2x2 and 2x2x4 reconstructions by varying temperature could be related to the change of distortion stacking along the c axis [48]. One important feature of a 3D CDW order is that the six-fold rotational symmetry can be broken for the distortions involving an in-plane π shift between adjacent layers. The SoD-TrH- π configuration can account for the observed two-fold symmetrical c -axis resistivity in experiments [39]. In addition, the 3D CDW order can also generate band folding along the c axis, providing a qualitatively better account for the double electron bands around the $\bar{\Gamma}$ point (Figs. 1e and 1g; Figs. 3c and 3f). While the DFT calculations based on static lattice distortions go a long way in reproducing our band structure

measurements in the CDW phase, they do not account for the time-reversal symmetry breaking seen in other experiments [32,35]. This suggests that electron-phonon coupling and electron-electron interactions may conspire to generate the unconventional CDW order in AV_3Sb_5 kagome metals, which deserves further investigations, both from the theoretical and the experimental side.

References:

- [1] M. R. Norman, Colloquium: Herbertsmithite and the search for the quantum spin liquid, *Rev. Mod. Phys.* **88**, 041002 (2016).
- [2] D. Wulferding, P. Lemmens, P. Scheib, J. Roder, P. Mendels, S. Chu, T. Han, and Y. S. Lee, Interplay of thermal and quantum spin fluctuations in the kagome lattice compound herbertsmithite, *Phys. Rev. B* **82**, 144412 (2010).
- [3] S. Yan, D. A. Huse, and S. R. White, Spin-Liquid Ground State of the $S = 1/2$ Kagome Heisenberg Antiferromagnet, *Science* **332**, 1173–1176 (2011).
- [4] T.-H. Han, J. S. Helton, S. Chu, D. G. Nocera, J. A. Rodriguez- Rivera, C. Broholm, and Y. S. Lee, Fractionalized excitations in the spin-liquid state of a kagome-lattice antiferromagnet, *Nature* (London) **492**, 406–410 (2012).
- [5] T. Han, S. Chu, and Y. S. Lee, Refining the Spin Hamiltonian in the Spin-1/2 Kagome Lattice Antiferromagnet $\text{ZnCu}_3(\text{OH})_6\text{Cl}_2$ Using Single Crystals, *Phys. Rev. Lett.* **108**, 157202 (2012).
- [6] M. Fu, T. Imai, T.-H. Han, and Y. S. Lee, Evidence for a gapped spin-liquid ground state in a kagome Heisenberg antiferromagnet, *Science* **350**, 655–658 (2015).
- [7] J.-X. Yin, S. S. Zhang, G. Chang, Q. Wang, S. S. Tsirkin, Z. Guguchia, B. Lian, H. Zhou, K. Jiang, I. Belopolski, N. Shumiya, D. Multer, M. Litskevich, T. A. Cochran, H. Lin, Z. Wang, T. Neupert, S. Jia, H. Lei, and M. Z. Hasan, Negative flat band magnetism in a spin-orbit- coupled correlated kagome magnet, *Nature Physics* **15**, 443–448 (2019).
- [8] W. -H. Ko, P. A. Lee, and X. -G. Wen, Doped kagome system as exotic superconductor, *Phys. Rev. B* **79**, 214502 (2009).
- [9] M. L. Kiesel, and R. Thomale, Sublattice interference in the kagome Hubbard model, *Phys. Rev. B* **86**, 121105(R) (2012).
- [10] M. L. Kiesel, C. Platt, and R. Thomale, Unconventional Fermi Surface Instabilities in the Kagome Hubbard Model, *Phys. Rev. Lett.* **110**, 126405 (2013).
- [11] W.-S. Wang, Z.-Z. Li, Y.-Y. Xiang, and Q.-H. Wang, Competing electronic orders on kagome lattices at van Hove filling, *Phys. Rev. B* **87**, 115135 (2013).
- [12] H.-M. Guo, and M. Franz, Topological insulator on the kagome lattice, *Phys. Rev. B* **80**, 113102 (2009).
- [13] S. Isakov, S. Wessel, R. Melko, K. Sengupta, and Y. B. Kim, Hard-Core Bosons on the Kagome Lattice: Valence-Bond Solids and Their Quantum Melting, *Phys. Rev. Lett.* **97**, 147202 (2006).

- [14] L. Ye, M. Kang, J. Liu, F. Cube, C. R. Wicker, T. Suzuki, C. Jozwiak, A. Bostwick, E. Rotenberg, D. C. Bell, L. Fu, R. Comin, and Joseph G. Checkelsky, Massive Dirac fermions in a ferromagnetic kagome metal, *Nature (London)* **555**, 638–642 (2018).
- [15] J.-X. Yin, W. Ma, T. A. Cochran, X. Xu, S. S. Zhang, H.-J. Tien, N. Shumiya, G. Cheng, K. Jiang, B. Lian, Z. Song, G. Chang, I. Belopolski, D. Multer, M. Litskevich, Z.-J. Cheng, X. P. Yang, B. Swidler, H. Zhou, H. Lin, T. Neupert, Z. Wang, N. Yao, T.-R. Chang, S. Jia, and M. Z. Hasan, Quantum-limit Chern topological magnetism in TbMn_6Sn_6 , *Nature (London)* **583**, 533–536 (2020).
- [16] M. Kang, L. Ye, S. Fang, J.-S. You, A. Levitan, M. Han, J. I. Facio, C. Jozwiak, A. Bostwick, E. Rotenberg, M. K. Chan, R. D. McDonald, D. Graf, K. Kaznatcheev, E. Vescovo, D. C. Bell, E. Kaxiras, J. Brink, M. Richter, M. P. Ghimire, J. G. Checkelsky, and R. Comin, Dirac fermions and flat bands in the ideal kagome metal FeSn , *Nat. Mater.* **19**, 163–169 (2020).
- [17] H. Tsai, T. Higo, K. Kondou, T. Nomoto, A. Sakai, A. Kobayashi, T. Nakano, K. Yakushiji, R. Arita, S. Miwa, et al., Electrical manipulation of a topological antiferromagnetic state, *Nature* **580**, 608–613 (2020).
- [18] B. R. Ortiz, L. C. Gomes, J. R. Morey, M. Winiarski, M. Bordelon, J. S. Mangum, I. W. Oswald, J. A. Rodriguez-Rivera, J. R. Neilson, S. D. Wilson, New kagome prototype materials: discovery of KV_3Sb_5 , RbV_3Sb_5 , and CsV_3Sb_5 , *Phys. Rev. Mater.* **3**, 094407 (2019).
- [19] B. R. Ortiz, S. M. Teicher, Y. Hu, J. L. Zuo, P. M. Sarte, E. C. Schueller, A. M. Abeykoon, M. J. Krogstad, S. Rosenkranz, R. Osborn, R. Seshadri, L. Balents, J. He, and S. D. Wilson, CsV_3Sb_5 : A \mathbb{Z}_2 Topological Kagome Metal with a Superconducting Ground State, *Phys. Rev. Lett.* **125**, 247002 (2020).
- [20] B. R. Ortiz, P. M. Sarte, E. M. Kenney, M. J. Graf, S. M. L. Teicher, R. Seshadri, and S. D. Wilson, Superconductivity in the \mathbb{Z}_2 kagome metal KV_3Sb_5 , *Phys. Rev. Mater.* **5**, 034801 (2021).
- [21] Q. Yin, Z. Tu, C. Gong, Y. Fu, S. Yan, and H. Lei, Superconductivity and Normal-State Properties of Kagome Metal RbV_3Sb_5 Single Crystals, *Chin. Phys. Lett.* **38**, 037403 (2021).
- [22] Y. Hu, S. M. L. Teicher, B. R. Ortiz, Y. Luo, S. Peng, L. Huai, J. Z. Ma, N. C. Plumb, S. D. Wilson, J.-F. He, and M. Shi, Charge-order-assisted topological surface states and flat bands in the kagome superconductor CsV_3Sb_5 , Preprint at arXiv:2104.12725 (2021).
- [23] M. G. Kang, S. Fang, J. Kim, B. R. Ortiz, S. H. Ryu, J. Kim, J. Yoo, G. Sangiovanni, D. D. Sante, B.-G. Park, C. Jozwiak, A. Bostwick, E. Rotenberg, E. Kaxiras, S. D. Wilson, J.-H. Park, and Riccardo Comin, Twofold van Hove singularity and origin of charge order in topological kagome superconductor CsV_3Sb_5 . Preprint at arXiv:2105.01689 (2021).

- [24] Y. Hu, X. Wu, B. R. Ortiz, S. Ju, X. Han, J. Z. Ma, N. C. Plumb, M. Radovic, R. Thomale, S. D. Wilson, A. P. Schnyder, and M. Shi, Rich nature of van Hove singularities in kagome superconductor CsV_3Sb_5 , Preprint at arXiv:2106.05922 (2021).
- [25] H. L. Luo, Q. Gao, H. Liu, Y. Gu, D. Wu, C. Yi, J. Jia, S. Wu, X. Luo, Y. Xu, L. Zhao, Q. Wang, H. Mao, G. Liu, Z. Zhu, Y. Shi, K. Jiang, J. Hu, Z. Xu, and X. J. Zhou, Electronic Nature of Charge Density Wave and Electron-Phonon Coupling in Kagome Superconductor KV_3Sb_5 , Preprint at arXiv:2107.02688 (2021).
- [26] M. M. Denner, R. Thomale, T. Neupert, Analysis of charge order in the kagome metal AV_3Sb_5 ($A=\text{K, Rb, Cs}$), *Phys. Rev. Lett.* **127**.217601 (2021).
- [27] C. C. Zhao, L. S. Wang, W. Xia, Q. W. Yin, J. M. Ni, Y. Y. Huang, C. P. Tu, Z. C. Tao, Z. J. Tu, C. S. Gong, H. C. Lei, Y. F. Guo, X. F. Yang, and S. Y. Li, Nodal superconductivity and superconducting domes in the topological Kagome metal CsV_3Sb_5 , Preprint at arXiv:2102.08356 (2021).
- [28] K. Y. Chen, N. N. Wang, Q. W. Yin, Z. J. Tu, C. S. Gong, J. P. Sun, H. C. Lei, Y. Uwatoko, and J.-G. Cheng, Double superconducting dome and triple enhancement of T_c in the kagome superconductor CsV_3Sb_5 under high pressure, *Phys. Rev. Lett.* **126**, 247001 (2021).
- [29] Z. Zhang, Z. Chen, Y. Zhou, Y. Yuan, S. Wang, L. Zhang, X. Zhu, Y. Zhou, X. Chen, J. Zhou, and Z. Yang, Pressure-induced Reemergence of Superconductivity in Topological Kagome Metal CsV_3Sb_5 , *Phys. Rev. B* **103**, 224513 (2021).
- [30] X. Chen, X. Zhan, X. Wang, J. Deng, X. -B. Liu, X. Chen, J. -G. Guo, and X. Chen, Highly-robust reentrant superconductivity in CsV_3Sb_5 under pressure, *Chin. Phys. Lett.* **38**, 057402 (2021).
- [31] Y. Wang, S.-Y. Yang, P. K. Sivakumar, B. R. Ortiz, S. M. L. Teicher, H. Wu, A. K. Srivastava, C. Garg, D. Liu, S. S. P. Parkin, E. S. Toberer, T. McQueen, S. D. Wilson, M. N. Ali, Proximity-induced spin-triplet superconductivity and edge supercurrent in the topological Kagome metal, $\text{K}_{1-x}\text{V}_3\text{Sb}_5$, Preprint at arXiv:2012.05898 (2020).
- [32] Y.-X. Jiang, J.-X. Yin, M. M. Denner, N. Shumiya, B. R. Ortiz, J. He, X.-X. Liu, S.-T. S. Zhang, G.-Q. Chang, I. Belopolski, Q. Zhang, T. A. Cochran, D. Multer, M. Litskevich, Z.-J. Cheng, X. P. Yang, Z. Wang, R. Thomale, T. Neupert, S. D. Wilson, and M. Zahid Hasan, Unconventional chiral charge order in kagome superconductor KV_3Sb_5 , *Nat. Mater.* **20**, 1353–1357 (2021).
- [33] H. Chen, B. Hu, Z. Zhao, J. Yuan, Y. Xing, G. Qian, Z. Huang, G. Li, Y. Ye, Q. Yin, C. Gong, Z. Tu, H. Lei, S. Ma, H. Zhang, S. Ni, H. Tan, C. Shen, X. Dong, B. Yan, Z. Wang, and H. -J. Gao, Roton pair density wave and unconventional strong-coupling superconductivity in a topological kagome metal, *Nature* **559**, 222–228(2021).

- [34] H. Zhao, H. Li, B. R. Ortiz, S. M. L. Teicher, T. Park, M. Ye, Z. Wang, L. Balents, S. D. Wilson, and I. Zeljkovic, Cascade of correlated electron states in a kagome superconductor CsV_3Sb_5 , *Nature* **599**, 216–221 (2021).
- [35] C. Mielke III, D. Das, J.-X. Yin, H. Liu, R. Gupta, C. N. Wang, Y.-X. Jiang, M. Medarde, X. Wu, H. C. Lei, J. J. Chang, P. Dai, Q. Si, H. Miao, R. Thomale, T. Neupert, Y. Shi, R. Khasanov, M. Z. Hasan, H. Luetkens, and Z. Guguchia, Time-reversal symmetry-breaking charge order in a correlated kagome superconductor, Preprint at arXiv:2106.13443 (2021).
- [36] S.-Y. Yang, Y. Wang, B. R. Ortiz, D. Liu, J. Gayles, E. Derunova, R. Gonzalez-Hernandez, L. Šmejkal, Y. Chen, S. S. P. Parkin, S. D. Wilson, E. S. Toberer, T. McQueen, and M. N. Ali, Giant, unconventional anomalous Hall effect in the metallic frustrated magnet candidate, KV_3Sb_5 , *Sci. Adv.* **6**, abb6003 (2020).
- [37] F. H. Yu, T. Wu, Z. Y. Wang, B. Lei, W. Z. Zhuo, J. J. Ying, and X. H. Chen, Concurrence of anomalous Hall effect and charge density wave in a superconducting topological kagome metal. *Phys. Rev. B* **104**, L041103 (2021).
- [38] H. Li, H. Zhao, B. R. Ortiz, T. Park, M. Ye, L. Balents, Z. Wang, S. D. Wilson, and I. Zeljkovic, Rotation symmetry breaking in the normal state of a kagome superconductor KV_3Sb_5 , Preprint at arXiv:2104.08209 (2021).
- [39] Y. Xiang, Q. Li, Y. Li, W. Xie, H. Yang, Z. Wang, Y. Yao, and H.-H. Wen, Twofold symmetry of c-axis resistivity in topological kagome superconductor CsV_3Sb_5 with in-plane rotating magnetic field. *Nat. Commun.* **12**, 6727 (2021).
- [40] H. Tan, Y. Liu, Z. Wang, and B. Yan, Charge density waves and electronic properties of superconducting kagome metals, *Phys. Rev. Lett.* **127**, 046401 (2021).
- [41] M. H. Christensen, T. Birol, B. M. Andersen, and R. M. Fernandes, Theory of the charge-density wave in AV_3Sb_5 kagome metals, Preprint at arXiv:2107.04546 (2021).
- [42] X. Wu, T. Schwemmer, T. Müller, A. Consiglio, G. Sangiovanni, D. D. Sante, Y. Iqbal, W. Hanke, A. P. Schnyder, M. M. Denner, M. H. Fischer, T. Neupert, and R. Thomale, Nature of unconventional pairing in the kagome superconductors AV_3Sb_5 , *Phys. Rev. Lett.* **127**, 177001 (2021).
- [43] Y.-P. Lin, and R. M. Nandkishore, Complex charge density waves at Van Hove singularity on hexagonal lattices: Haldane-model phase diagram and potential realization in kagome metals AV_3Sb_5 , *Phys. Rev. B* **104**, 045122 (2021).
- [44] T. Park, M. Ye, and L. Balents, Electronic instabilities of kagome metals: saddle points and Landau theory, *Phys. Rev. B* **104**, 035142 (2021).

- [45] H. X. Li, T. T. Zhang, Y.-Y. Pai, C. Marvinney, A. Said, T. Yilmaz, Q. Yin, C. Gong, Z. Tu, E. Vescovo, R. G. Moore, S. Murakami, H. C. Lei, H. N. Lee, B. Lawrie, and H. Miao, Observation of Unconventional Charge Density Wave without Acoustic Phonon Anomaly in Kagome Superconductors AV_3Sb_5 ($A=Rb, Cs$), *Phys. Rev. X* **11**, 031050 (2021).
- [46] Z. Liang, X. Hou, F. Zhang, W. Ma, P. Wu, Z. Zhang, F. Yu, J. -J. Ying, K. Jiang, L. Shan, Z. Wang, X. -H. Chen, Three-dimensional charge density wave and robust zero-bias conductance peak inside the superconducting vortex core of a kagome superconductor CsV_3Sb_5 , *Phys. Rev. X* **11**, 031026 (2021).
- [47] B. R. Ortiz, S. M. L. Teicher, L. Kautzsch, P. M. Sarte, J. P. C. Ruff, R. Seshadri, and S. D. Wilson, Fermi surface mapping and the nature of charge density wave order in the kagome superconductor CsV_3Sb_5 , *Phys. Rev. X* **11**, 041030 (2021).
- [48] Q. Stahl, D. Chen, T. Ritschel, C. Shekhar, C. Felser, and J. Geck, Temperature-driven reorganization of electronic order in CsV_3Sb_5 , Preprint at arXiv:2112.02559 (2021).
- [49] J. Luo, Z. Zhao, Y. Z. Zhou, J. Yang, A. F. Fang, H. T. Yang, H. J. Gao, R. Zhou, and G.-Q. Zheng, Star-of-David pattern charge density wave with additional modulation in the kagome superconductor CsV_3Sb_5 revealed by ^{51}V -NMR and $^{121/123}Sb$ -NQR, Preprint at arXiv:2108.10261 (2021).
- [50] K. Nakayama, Y. Li, T. Kato, M. Liu, Z. Wang, T. Takahashi, Y. Yao, and T. Sato, *Phys. Rev. B* **104**, L161112 (2021).
- [51] Y. Cai, Y. Wang, Z. Hao, Y. Liu, X.-M. Ma, Z. Shen, Z. Jiang, Y. Yang, W. Liu, Q. Jiang, Z. Liu, M. Ye, D. Shen, Z. Sun, J. Chen, L. Wang, C. Liu, J. Lin, J. Wang, B. Huang, J.-W. Mei, and C. Chen, Emergence of Quantum Confinement in Topological Kagome Superconductor CsV_3Sb_5 family, Preprint at arXiv:2109.12778 (2021).
- [52] Y. Luo, S. Peng, S. M. L. Teicher, L. Huai, Y. Hu, B. R. Ortiz, Z. Wei, J. Shen, Z. Ou, B. Wang, Y. Miao, M. Guo, M. Shi, S. D. Wilson, and J.-F. He, Distinct band reconstructions in kagome superconductor CsV_3Sb_5 , Preprint at arXiv:2106.02688 (2021).
- [53] G. Kresse, and J. Hafner, Ab initio molecular dynamics for liquid metals, *Phys. Rev. B* **47**, 558–561 (1993).
- [54] G. Kresse, and J. Furthmüller, Efficiency of ab-initio total energy calculations for metals and semiconductors using a plane-wave basis set, *Computational Materials Science* **6**, 15–50 (1996).
- [55] G. Kresse, and J. Furthmüller, Efficient iterative schemes for ab initio total-energy calculations using a plane-wave basis set, *Phys. Rev. B* **54**, 11169 (1996).
- [56] J. P. Perdew, K. Burke, and M. Ernzerhof, Generalized Gradient Approximation Made Simple, *Phys. Rev. Lett.* **77**, 3865 (1996).

- [57] H. J. Monkhorst, and J. D. Pack, Special points for Brillouin-zone integrations, *Phys. Rev. B* **13**, 5188 (1976).
- [58] S. Grimme, J. Antony, S. Ehrlich, and H. Krieg, A consistent and accurate ab initio parametrization of density functional dispersion correction (DFT-D) for the 94 elements H-Pu, *J. Chem. Phys.* **132**, 154104 (2010).
- [59] V. Popescu, and A. Zunger, Extracting E versus k effective band structure from supercell calculations on alloys and impurities, *Phys. Rev. B* **85**, 085201 (2012).
- [60] P. V. C. Medeiros, Sven Stafström, and Jonas Björk, Effects of extrinsic and intrinsic perturbations on the electronic structure of graphene: Retaining an effective primitive cell band structure by band unfolding, *Phys. Rev. B* **89**, 041407 (2014).

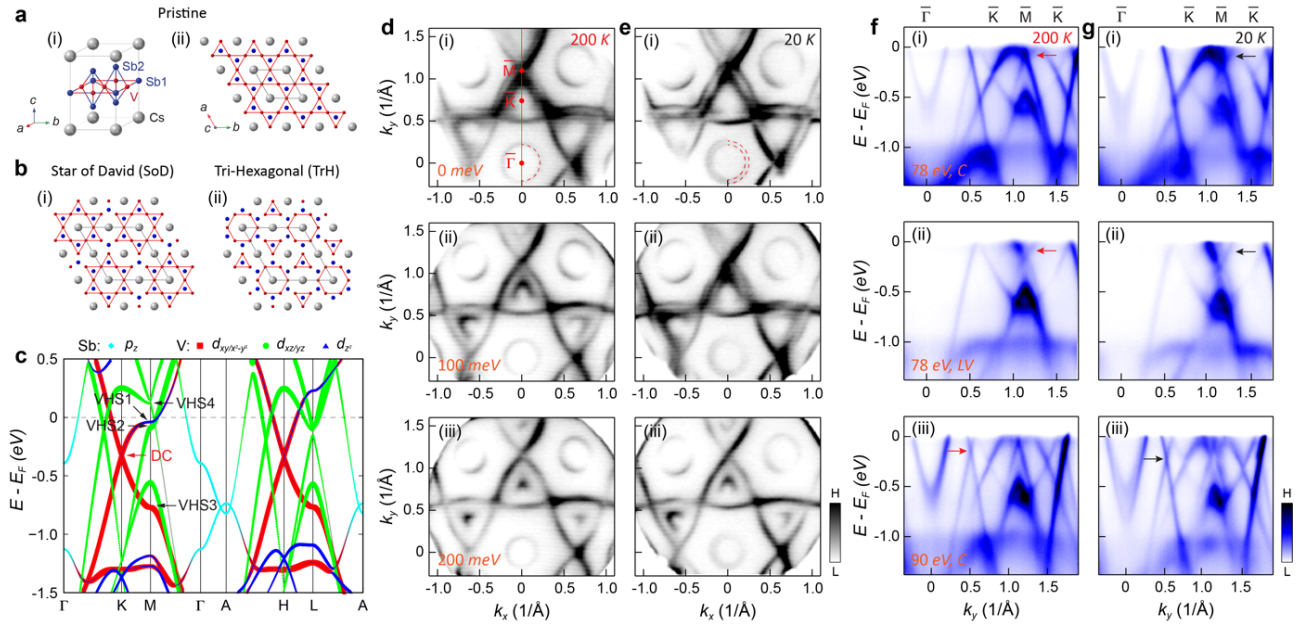


Fig. 1 | Crystal and electronic structures of the kagome superconductors CsV₃Sb₅ above and below T_{CDW} . **a** Crystal structure of CsV₃Sb₅ in the normal state ($T > T_{CDW}$), showing the unit cell in 3D (i), along with the kagome arrangement of vanadium atoms in the *a-b* plane (ii). **b** The crystal structure in the CDW phase ($T < T_{CDW}$) with the candidate Star of David structure (SoD, i) and Tri-Hexagonal structure (TrH, ii). **c** DFT calculations for the orbital character resolved band structure of CsV₃Sb₅. The orange arrow indicates the Dirac cone (DC) at the K point. **d** Fermi surface (i), constant energy contours at binding energies (E_B) of 100 meV (ii), and 200 meV (iii), at 200 K. **e** Same as (d), but taken at 20 K. The red dashed line is the guide to the eye for the electron pocket contributed by the Sb p_z -orbital. **f** ARPES spectra obtained at 200 K, measured with 78 eV circular (C) polarization (i), 78 eV linear vertical (LV) polarization (ii), and 90 eV C polarization (iii), taken along the $\bar{\Gamma} - \bar{K} - \bar{M} - \bar{K}$ direction as indicated by the red line in [d(i)]. **g** Same as (f), but measured at 20 K. The red and black arrows in (f) and (g) highlight the distinct band dispersions above and below the T_{CDW} , respectively.

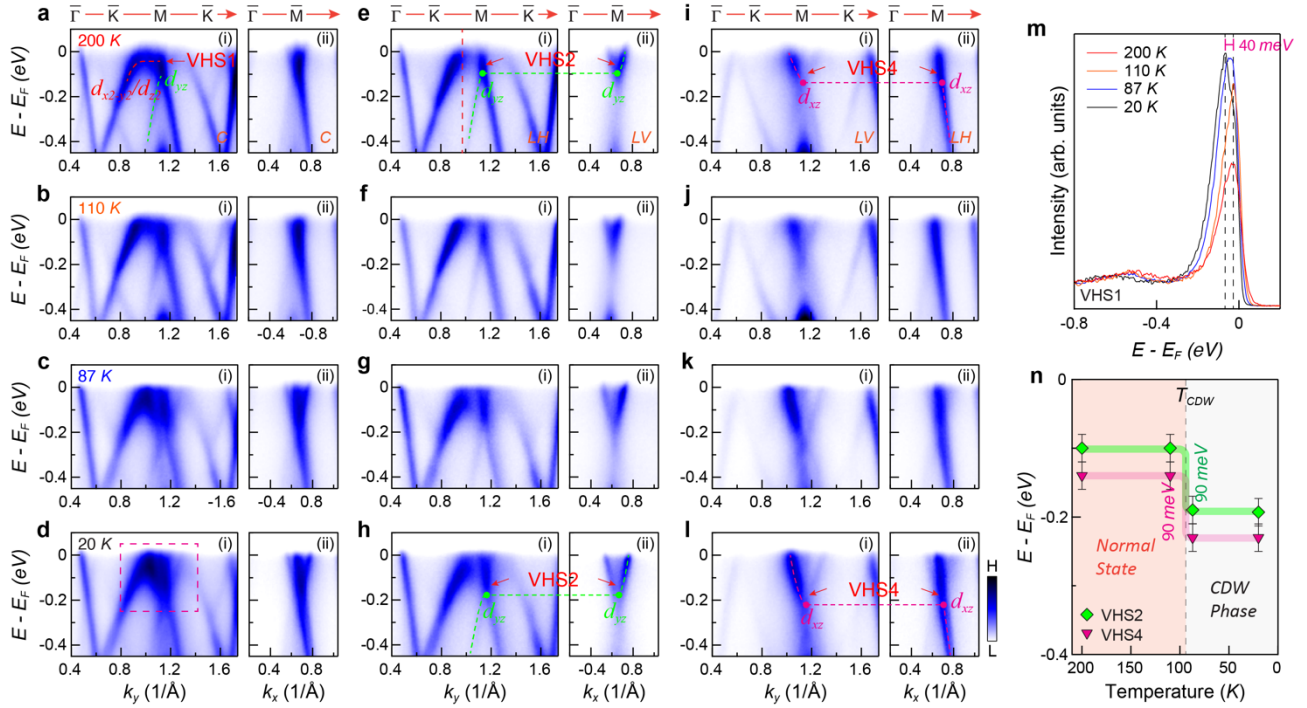


Fig. 2 | Temperature and polarization dependence of the electronic structure in CsV₃Sb₅. a-d ARPES spectra taken along the $\bar{\Gamma} - \bar{K} - \bar{M} - \bar{K} - \bar{\Gamma}$ [left panel, (i)] and $\bar{\Gamma} - \bar{M} - \bar{\Gamma}$ [right panel, (ii)] directions, respectively, measured at 200 K (a), 110 K (b), 87 K (c), 20 K (d) with 78 eV C polarized light. e-h, i-l Same as (a-d), but obtained with linear horizontal (LH) [e-h(i), i-l(ii)] and LV [e-h(ii), i-l(i)] polarizations. The dashed curves in (a, e, h, i, l) are guides to the eye for the kagome bands around the \bar{M} point. The red arrow indicates the VHSs. m Temperature evolution of the energy distribution curves (EDCs) taken around the flat feature of VHS1. The position of the EDCs is indicated by the red dashed line in e(i). n Energy location of VHS2 and VHS4 as a function of temperature.

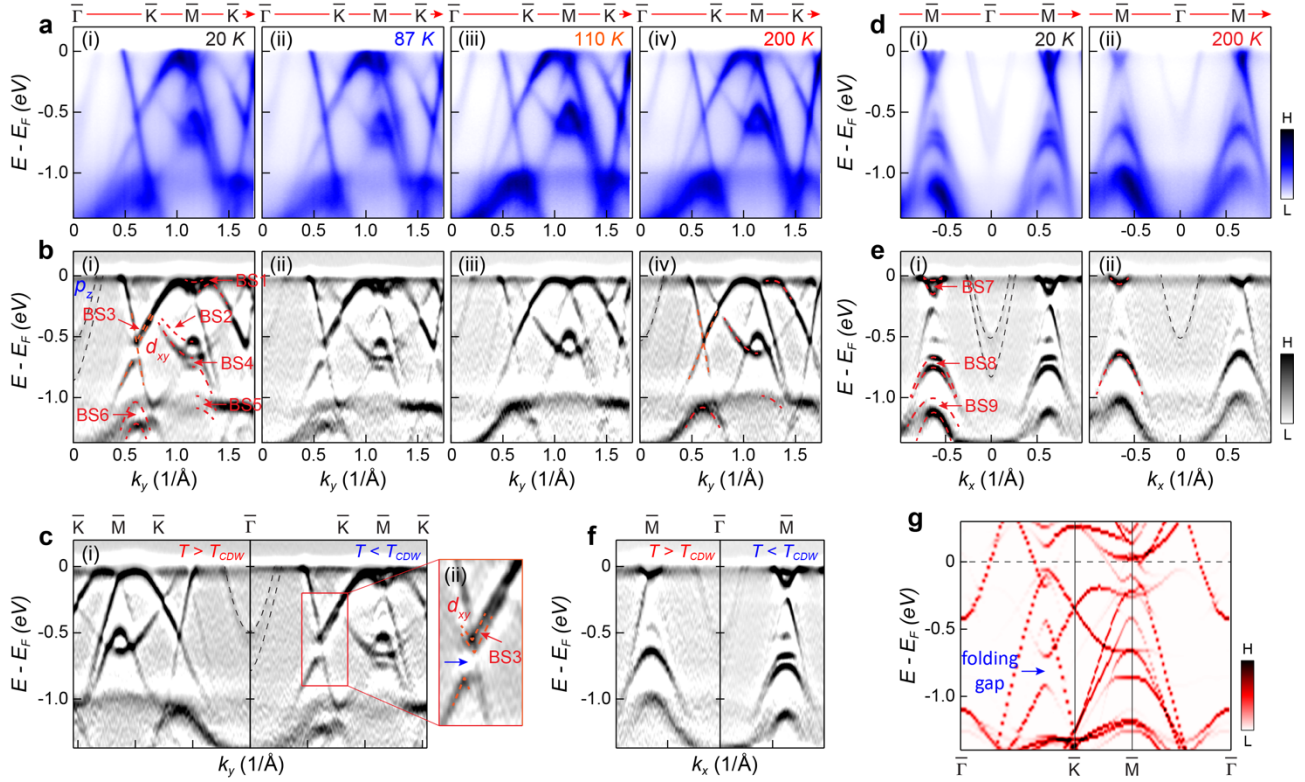


Fig. 3 | Double-band splitting features of the kagome bands below T_{CDW} . **a,b** ARPES spectra (a) and their curvature plots (b) at different temperatures, taken along the $\bar{\Gamma} - \bar{K} - \bar{M}$ direction. **c** Comparison of the curvature plots taken above T_{CDW} (200 K) and below T_{CDW} (20 K). Orange box in (i) highlights the folding gap on the d_{xy} orbital (ii). **d-f** Same as (a-c), but measured along the $\bar{\Gamma} - \bar{M}$ direction. The green and red dashed lines are guides to the eye for the kagome bands in the normal state and CDW phase, respectively. The red arrows indicate the double-band splittings on kagome bands in the CDW phase, marked as BS1-BS9. **g** DFT calculations for the unfolded band structures of 2x2 TrH phase. The blue arrow in [c(ii)] and (g) indicate the CDW associated folding gap.

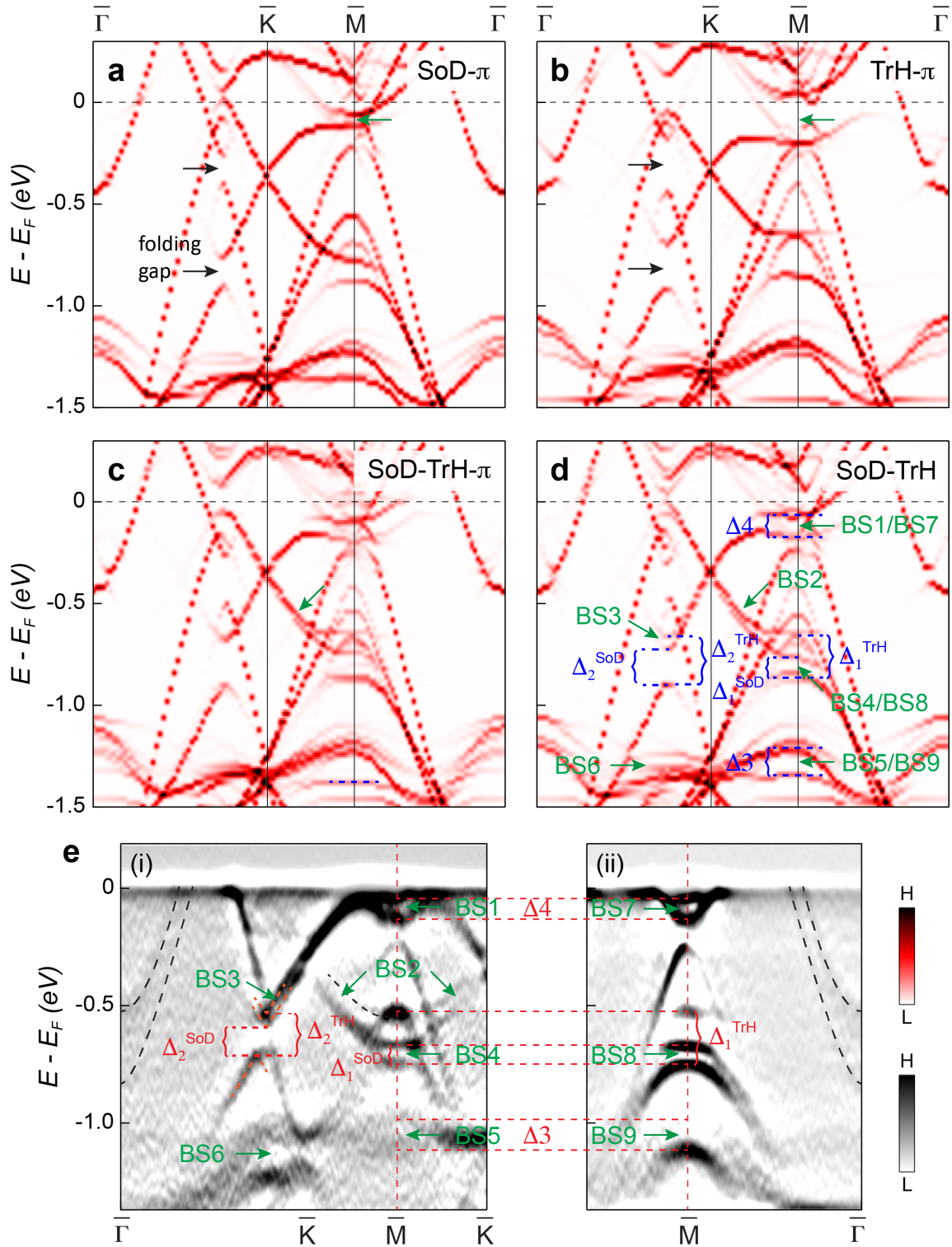


Fig. 4 | Unfolded band structures of CsV_3Sb_5 in $2 \times 2 \times 2$ CDW order from DFT calculations and their comparison with experiments. a-d The unfolded band structures of the following lattice configurations: SoD- π (a), TrH- π (b), SoD-TrH- π (c), and SoD-TrH (d). The blue dashed lines define the splitting gaps ($\Delta_1, \Delta_3, \Delta_4$) and folding gaps (Δ_2). The superscripts SoD and TrH in the gaps (Δ_1, Δ_2) represent the contributions of the two configurations, respectively. **e** ARPES spectra taken at 20 K along the $\bar{\Gamma} - \bar{K} - \bar{M}$ direction (i) and the $\bar{\Gamma} - \bar{M}$ direction. The green arrow indicates the observed band reconstructions (marked as BS1-BS9) in the CDW phase.